Brownmillerite-Type Sr 2 ScGaO 5 Oxide Ion Conductor: Local Structure, Phase Transition, and Dynamics

Chloe A Fuller, Quentin Berrod, Bernhard Frick, Mark Johnson, Stewart J Clark, John S. O. Evans, Ivana Radosavljevic Evans

CHEMISTRY OF MATERIALS
Cite This: Chem. Mater. 2019, 31, 7395−7404
Article
pubs.acs.org/cm

Brownmillerite-Type Sr_2ScGaO_5 Oxide Ion Conductor: Local Structure, Phase Transition, and Dynamics

Chloe A. Fuller,[†] Quentin Berrod,[‡] Bernhard Frick,[§] Mark R. Johnson,[§] Stewart J. Clark,[∥] John S. O. Evans,*[,†] and Ivana Radosavljevic Evans*[,†]

[†]Department of Chemistry, Durham University, Science Site, South Road, Durham DH1 3LE, United Kingdom
[‡]CNRS-CEA-Université Grenoble Alpe SyMMES, 38000 Grenoble, France
[§]Institut Laue Langevin, 71 Rue de Martyrs, 38000 Grenoble, France
[∥]Department of Physics, Durham University, Science Site, South Road, Durham DH1 3LE, United Kingdom

Supporting Information

ABSTRACT: Brownmillerite-type Sr_2ScGaO_5 has been investigated by a range of experimental X-ray and neutron scattering techniques (diffraction, total scattering, and spectroscopy) and density functional theory calculations in order to characterize its structure and dynamics. The material undergoes a second-order phase transition on heating during which a rearrangement of the $(GaO_{4/2})_\infty$ tetrahedral chains occurs, such that they change from being essentially fully ordered in a polar structure at room temperature to being orientationally disordered above 400 °C. Pair distribution function analysis carried out using neutron total scattering data suggests that GaO_4 tetrahedra remain as fairly rigid units above and below this transition, whereas coordination polyhedra in the $(ScO_{6/2})_\infty$ layers distort more. Inelastic neutron scattering and phonon calculations reveal the particular modes that are associated with this structural change, which may assist ionic conductivity in the material at higher temperatures. On the basis of the correlations between these findings and the measured conductivity, we have synthesized a derivative compound with increased conductivity and suggest a possible conduction mechanism in these brownmillerite-type solid electrolytes.

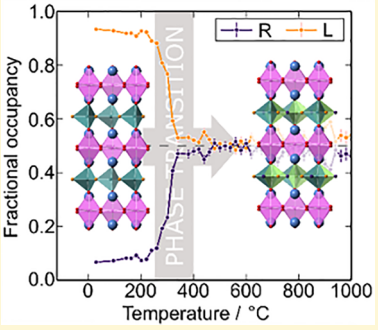

INTRODUCTION

The brownmillerite-type mixed metal oxides of general formula $A_2B_2O_5$ are chemically versatile compounds studied for exploitable properties that include fast ion conduction (oxide ion and proton), electrocatalysis, sensing, and photoluminescence.[1−5] The structure can be described as oxygen-deficient perovskite with one-sixth of the oxide ions replaced by vacancies. The vacancies are crystallographically ordered along one direction resulting in alternating, corner-sharing octahedral and tetrahedral layers containing $BO_{6/2}$ and $BO_{4/2}$ coordination polyhedra, respectively. Within the tetrahedral layers, BO_4 tetrahedra are arranged such that they form 1-dimensional chains along the *a*-axis (Figure 1) of the $\sqrt{2}\,a_p \times 4a_p \times \sqrt{2}\,a_p$ (a_p = perovskite cell) orthorhombic unit cell.

Depending on the composition, atmosphere, and temperature, brownmillerite-type materials can exhibit oxide ion, mixed ionic-electronic, or proton conductivity. At elevated temperatures, many undergo phase transitions in which vacancies become disordered, and this is often accompanied by a marked increase in oxide ion conductivity. For example, $Ba_2In_2O_5$ is a moderate oxide ion conductor ($\sim 10^{-4}$ S cm^{-1} at 600 °C)[1] before it undergoes a structural phase transition to tetragonal and eventually to cubic perovskite[6] above 900 °C, when its conductivity increases to 0.1 S cm^{-1}. Replacing half the In atoms with Ga results in the formation of Ba_2InGaO_5 with the B-site cations ordered and a lower conductivity relative to $Ba_2In_2O_5$ (10^{-6} S cm^{-1} at 600 °C).[7] Ionic conductivity of up to 5×10^{-3} S cm^{-1} at 600 °C has been found in the $Ba_2GdIn_{1-x}Ga_xO_5$ (x = 0, 0.2, 0.4) series,[8] and even better performance has been reported for Ga-doped $Ba_2(In_{1-x}Ga_x)_2O_5$ (x = 0−0.45) materials, although for $x \geq 0.25$ these adopt a cubic perovskite-type structure.[9]

$Ca_2Fe_2O_5$ and $Sr_2Fe_2O_5$ also adopt the brownmillerite structure. They have been described as promising, low-temperature oxide ion conductors[10,11] because of their ability to intercalate oxygen under mild conditions (<100 °C with NaBrO/NaClO),[12,13] but the ionic conductivity at low temperatures remains unreported. The conductivity at high temperature, however, has been investigated and shows that $Ca_2Fe_2O_5$ and $Sr_2Fe_2O_5$ are mixed conductors with the moderate to high oxide ion components of 2×10^{-3} and 0.2 S cm^{-1} at 900 °C, respectively.[14−16] Possible ionic conduction mechanisms have been linked to a low-energy phonon mode that causes the destabilization of the apical oxygen (O2 in Figure 1).[10] High-temperature density functional theory (DFT) molecular dynamics (above 600 °C) showed that movement of this oxygen can then trigger the reorientation of

Received: May 24, 2019
Revised: August 5, 2019
Published: August 6, 2019

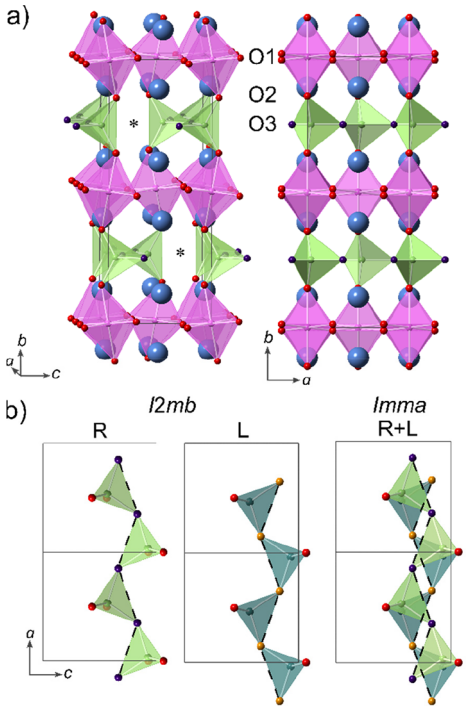

Figure 1. (a) Brownmillerite-type structure of Sr_2ScGaO_5 where green and pink polyhedra show $GaO_{4/2}$ and $ScO_{6/2}$ units, respectively, and the blue spheres show Sr ions. Red spheres indicate O ions, and purple is used to highlight the oxygens in the tetrahedral layer (O3). The vacancy channels are labeled with asterisks. (b) Different chain ordering patterns with right-pointing chains shown in light green with purple O and left-pointing chains shown in dark green and orange O. Note that all oxide ions are 2-coordinate.

$(FeO_{4/2})_\infty$ chains to provide a long-range diffusion pathway in $Sr_2Fe_2O_5$.[17]

Sr_2ScGaO_5 was first reported by Chernov et al. as a potential purely ionic conductor because of the fixed oxidation states of its components. It was described in orthorhombic space group *Icmm* (nonstandard setting of *Imma*), consistent with $(GaO_{4/2})_\infty$ chains disordered with respect to their orientation (left-handed, L, and right-handed, R; Figure 1b).[18] A subsequent study by Corallini et al.[11] described room-temperature Sr_2ScGaO_5 in the noncentrosymmetric polar space group *I2mb* (nonstandard setting of *Ima*2), in which the tetrahedral $(GaO_{4/2})_\infty$ chains are completely ordered (Figure 1).

Using powder neutron diffraction data collected at seven temperatures between room temperature and 1000 °C, Corallini et al. demonstrated that Sr_2ScGaO_5 (SSGO) undergoes a structural phase transition somewhere between 250 and 500 °C from space group *I2mb* to *Imma*, accompanied by the disordering of the tetrahedral chains into an arrangement that can be viewed as a superposition of the two possible orientations of the room-temperature polar structure. The authors report that this phase transition between the two orthorhombic SSGO forms manifests itself in the intensity change of just the (112) Bragg peak in their neutron diffraction data (showing that it mainly involves changes in the positions of oxygen atoms in the structure). $^{18}O/^{16}O$ isotope exchange measurements revealed the onset of oxygen mobility at ∼550 °C, which was correlated with the *I2mb* to *Imma* phase transition, i.e., the disordering of the tetrahedral chains in the structure. DFT molecular dynamics simulations carried out on Sr_2ScGaO_5 showed the reorientations of the $(GaO_{4/2})_\infty$ tetrahedral chains, i.e., switching between the L and R configurations occurred at 600 °C, accompanied by concerted movement of the O atoms from one equatorial position to the next, potentially leading to one-dimensional oxide ion diffusion along the crystallographic *a*-axis.[11] The apical O2 oxygen that was key in $Sr_2Fe_2O_5$ was not observed to be mobile in these simulations.

Around 1500 °C, Sr_2ScGaO_5 undergoes a further phase transition to the disordered cubic perovskite structure indicated by significant changes in the X-ray diffraction pattern.[19] Attempts to grow single crystals of Sr_2ScGaO_5 using the floating-zone method resulted in this cubic phase, which then persisted down to room temperature. Limited impedance measurements on the single crystal have shown that its conductivity is $\sim 10^{-5}$ S cm^{-1} at 400 °C, similar to that of powdered, orthorhombic $Ba_2In_2O_5$.[19]

Despite brownmillerite-type Sr_2ScGaO_5 being referred to as a pure oxide ion conductor and a very promising electrolyte in the literature,[19,20] we are unaware of conductivity measurements published on the orthorhombic form. The aim of this work was to determine the conductivity of brownmillerite-type Sr_2ScGaO_5 and correlate its dynamics to the average and local structure as a function of temperature. We have used a combination of experimental methods—variable-temperature neutron scattering studies (total scattering and inelastic and quasielastic scattering), impedance measurements, and phonon calculations to elucidate the structure−property relationships in Sr_2ScGaO_5. In addition, we report the derived phase, $Sr_2Sc_{0.95}Zn_{0.05}GaO_{4.975}$, in which the conductivity is ∼2 orders of magnitude higher than that in Sr_2ScGaO_5.

EXPERIMENTAL SECTION

Synthesis. Powder samples of Sr_2ScGaO_5 (SSGO) and $Sr_2Sc_{0.95}Zn_{0.05}GaO_{4.975}$ (SSGO-5%Zn) were synthesized from stoichiometric amounts of $SrCO_3$ (Fisher Chemical, >99.9%), Sc_2O_3 (Sigma-Aldrich, >99.9%), Ga_2O_3 (Sigma-Aldrich, >99.99%), and ZnO (Alfa Aesar, >99.99%). The oxides were mixed together in an agate pestle and mortar and heated at 1200 °C. Samples were reground, pressed into 10 mm pellets, and heated at the same temperature for a further 24 h. This was repeated until a single-phase product was obtained. Powder X-ray diffraction (PXRD), on a Bruker D8 Advance with a Lynx-eye detector and Cu Kα radiation, was used to monitor the progress of the solid-state reactions. For accurate cell parameter determination, PXRD was performed on the same instrument in a 2θ range $10° \leq 2\theta \leq 120°$ for 2 h, using a Si internal standard (a = 5.431195(9) Å at room temperature). Analysis of all diffraction data was carried out by the Rietveld method[21] implemented in the Topas Academic software.[22,23]

Chemical Analysis. The elemental composition of SSGO was measured by inductively coupled plasma mass spectrometry (ICP-MS) analysis performed on ∼50 mg of powdered sample dissolved in nitric acid using a Thermo Scientific Neptune Plus Higher Resolution Multicollector.

Thermogravimetric Analysis. Any mass losses that occurred in SSGO on heating were recorded in air on a PerkinElmer TGA 8000 instrument. Two different samples were heated from 30 to 600 °C at 10 °C min^{-1}.

Variable-Temperature X-ray Diffraction. PXRD patterns were recorded in air over a temperature range of 25−1000 °C on a Bruker D8 Advance (Lynx-eye detector, Cu Kα radiation) with an Anton Paar HTK1200 furnace attachment. Data were collected every 20 °C on heating and cooling, and patterns were analyzed by Rietveld fitting in Topas Academic.[22,23] Furnace temperatures were calibrated based on an external Al_2O_3 standard.[24]

DOI: 10.1021/acs.chemmater.9b02051
Chem. Mater. 2019, 31, 7395−7404

Neutron Diffraction and Total Scattering. A ∼6 g powder sample of SSGO was used to collect neutron total scattering data on the POLARIS instrument at the ISIS facility at Rutherford Appleton Laboratory. The sample was loaded and packed into an 8 mm diameter V can. High-quality data sets for pair distribution function (PDF) analysis were acquired at room temperature (6 sets of 175 μAh collections, 6 h) and 1000 °C (4 sets of 175 μAh collections, 4 h). The scattering due to the empty furnace and the empty can were measured at room temperature for 1 h each for background subtraction. In addition, 4 min data sets were collected at 45 temperatures on heating. Neutron total scattering data were normalized onto an absolute scale using GudrunN software,[25] and Bragg data were extracted using the established analysis routines in Mantid.[26] Rietveld and large-box local structure analyses were performed using Topas Academic.[22,23] RMCProfile[27] was used to confirm the local structure models and gave good fits to $F(Q)$ in addition to PDF and Bragg data.

The three highest resolution data banks (banks 3, 4, and 5) of POLARIS were used for variable-temperature neutron refinements and covered a d-spacing range of 0.15−5.75 Å. Bank 3 was used for joint PDF/Bragg analysis as it offers a good compromise between resolution and d-spacing range. For large-box fitting, PDF patterns were calculated using a 20 736-atom approximately isotropic box, and the Bragg scattering was calculated by folding the large-box coordinates back into a single crystallographic unit cell. In initial refinement cycles (both data sets fitted simultaneously), coordinate changes were constrained to prevent large atomic shifts; these constraints were relaxed during fitting. An equal weighting was applied to each point in the PDF such that the PDF and Bragg data gave a similar contribution to the overall χ^2. Large-box refinements converged within a couple of hours on a standard desktop PC. To avoid impurity peaks influencing the average structure of the large-box models, the peaks due to small amounts of Sc_2O_3 and $Sr_{10}Sc_4Ga_6O_{25}$ impurities were subtracted from the Bragg data before fitting.

Inelastic and Quasielastic Neutron Scattering. Inelastic neutron scattering data were collected on the time-of-flight spectrometer IN6 and on the backscattering spectrometer IN16B at the Institut Laue Langevin. The IN6 experiment was performed with an incident neutron wavelength of 5.12 Å and an elastic energy resolution of 70 μeV. A 10 g sample of SSGO was placed in a cylindrical, 8 mm diameter Nb sample holder, and data were collected at 77, 200, 400, 600, 800, and 1000 °C, with a collection time of 6 h at each temperature. Background scattering from the empty sample holder was measured for 6 h at room temperature. Vanadium was measured at 20 °C for 6 h for normalization and to describe the instrument resolution function.

The IN16B experiment was carried out with an incident neutron wavelength of 6.271 Å and an energy resolution of 0.75 μeV, to give access to nanosecond dynamics. A 10 g powdered sample was placed in a cylindrical 8 mm diameter Nb sample holder. Initially the measurements of elastic intensity (E = 0 μeV) and inelastic intensity at 2 μeV, were performed on heating from 20 to 900 °C using a heating rate of 0.04 °C s^{-1} and on cooling to 290 °C. Data points were collected in pairs with elastic intensity (EFWS—elastic fixed window scan) measured for 30 s, immediately followed by an inelastic intensity (IFWS—inelastic fixed window scan) measurement lasting 2 min.[28] Quasielastic neutron scattering (QENS) measurements were performed at room temperature and 1000 °C for 6 h at each temperature (as six 1-h repetitions) within an energy transfer window of ±20 μeV. The background scattering from the empty can was measured for 5 h, and a resolution function from a standard vanadium sample was also acquired at room temperature. The data from both experiments were analyzed using the LAMP software.[29]

Impedance Spectroscopy. Samples of SSGO and $Sr_2Sc_{0.95}Zn_{0.05}GaO_{4.975}$ (SSGO-5%Zn) were uniaxially pressed into 10 mm pellets and sintered for 24 h at 1200 °C. The resulting pellets were 74% and 71% of their theoretical density, respectively. Platinum paste was applied, and pellets were mounted on a Probostat A-6 cell and fired at 1000 °C for 1 h to set the electrodes. Impedance spectra were recorded in air, O_2, dry N_2, and wet N_2 using a Solartron 1260 frequency-response analyzer using frequency ranges of 0.1−10^7 Hz and voltages of 100−2500 mV. The temperature range of 200−1000 °C was sampled and the pellets were equilibrated for 20 min at each temperature before measurement.

Phonon Calculations. A geometry optimization and subsequent phonon calculation was performed on an $I2mb$ Sr_2ScGaO_5 model using the DFT methodologies implemented in CASTEP.[30,31] The calculations used the GGA-PBE exchange-correlation functional,[32] and treatment of the core electrons was done with accurate pseudopotentials.[33] A plane-wave energy cutoff of 1650 eV and 3 × 1 × 3 Monkhurst-Pack grid for k-point sampling was sufficient for differences in energy and forces to convergence to better than 1 meV $atom^{-1}$ and better than 1 meV $Å^{-1}$, respectively. The geometry optimization was performed on a fixed unit cell using the LBFGS minimization algorithm. Ions were allowed to relax until the residual forces on them were <0.01 eV $Å^{-1}$. The phonon calculation used linear response density functional perturbation theory performed on this geometry optimized model on a q-point grid of 3 × 1 × 3. Frequencies for the phonon density of states (PDOS) were calculated by interpolating on a fine grid with grid spacing 0.005 $Å^{-1}$. The phonon modes were visualized in Jmol.[34]

RESULTS AND DISCUSSION

Room-Temperature Average Structure. SSGO was successfully synthesized by a solid-state method; phase purity was confirmed by PXRD (see Supporting Information), and the elemental composition was found to be $Sr_2Sc_{1.02}Ga_{1.05}O_{5.11}$ by ICP-MS. The PXRD pattern was fitted with the $I2mb$ structure reported by Corallini et al.,[11] yielding an excellent agreement with an R_{wp} of 3.95%. Cell parameters were determined to be a = 5.7000(1) Å, b = 15.1409(3) Å, and c = 5.9115(1) Å at ambient temperature using a Si internal standard. The average structure was studied in more detail using neutron diffraction data. For the neutron studies, the synthesis was scaled up to 10 g, which introduced small amounts (<7% in total) of Sc_2O_3 and $Sr_{10}Sc_4Ga_6O_{25}$, a tetragonal phase reported by Chernov et al.[18] Rietveld fits are shown in Figure 2, and refined coordinates are given in the Supporting Information. Refinement of Sc/Ga site occupancies suggested full cation ordering (within 3%), in agreement with previous studies.[11,18]

Nonambient Structure. No new peaks nor any peak splitting was observed in the PXRD patterns of SSGO collected between 25 and 1000 °C (heating and cooling), indicating that no major structural changes occur. This is in line with the previous reports discussed in the Introduction. The (112) reflection was still present in the high-temperature X-ray data, in agreement with the results of Corallini et al.[11] The cell parameters, obtained from Rietveld fitting (Figure 3), show a smooth increase with temperature and no discernible hysteresis between heating and cooling cycles; however, there is a small departure from the smooth trend between 250 and 400 °C. This is more apparent in the thermal expansion coefficients, which reveal clear changes in the expansion of all three crystallographic axes between 250 and 400 °C. We note that the zinc-doped sample (SSGO-5%Zn) discussed later showed very similar thermal expansion behavior, with changes in thermal expansion at essentially identical temperatures. These data are included in the Supporting Information.

Similar cell parameter evolution was also seen in the neutron diffraction data of SSGO with the departure from the smooth trend appearing at the same temperature. In addition, the diffraction patterns suggest a phase transition between 260 and 340 °C characterized mainly by the disappearance of the (112) and (121) reflections (Supporting Information, Figure S3).

DOI: 10.1021/acs.chemmater.9b02051
Chem. Mater. 2019, 31, 7395−7404

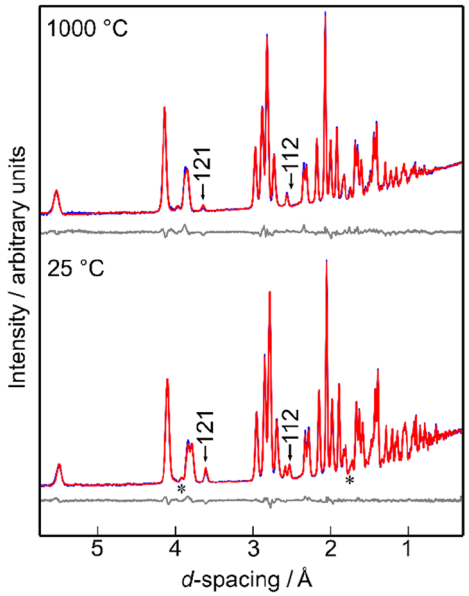

Figure 2. Rietveld fits of the powder neutron diffraction pattern of SSGO recorded on POLARIS (bank 3, d = 0.3−5.75 Å). Blue, red, and gray curves show the observed, calculated, and difference curves, respectively. The main peaks due to impurities have been highlighted with asterisks, and the SSGO peaks with the largest changes between low and high temperature are labeled.

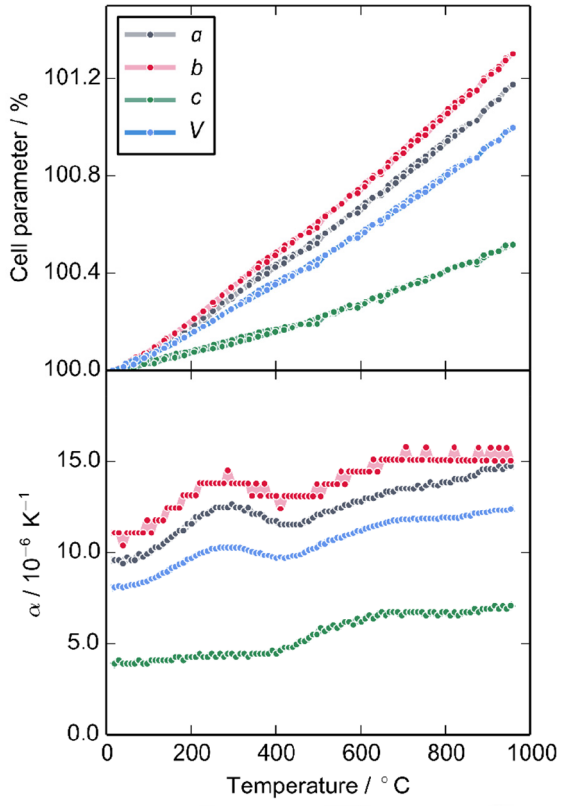

Figure 3. (Top) Evolution of the cell parameters with temperature expressed as a percentage of their room-temperature values. Cell parameters from both heating and cooling VTXRD experiments are plotted. Volume data are expressed as $V^{1/3}$. (Bottom) Thermal expansion behavior of each cell parameter. For the volume thermal expansion, we plot $1/3\alpha_V$.

This occurs within the temperature range of the change in thermal expansion behavior derived from PXRD measurements, and it is therefore likely that both observations relate to the same process. The neutron data were fitted with both *I*2*mb* and *Imma* models and, while both gave reasonable fits (R_{wp} = 3−4%) across the temperature range, the *I*2*mb* model visibly overestimated the (112) and (121) reflections at high temperature, confirming that the intensities of these peaks reflect the $(GaO_{4/2})_\infty$ chain disorder.

To elucidate the structural changes occurring in this temperature region, the variable-temperature neutron diffraction data were fitted using a model that allowed the Ga and O3 atoms corresponding to both L and R orientations to be present. Their fractional occupancies were refined using data from POLARIS banks 3−5 and are plotted in Figure 4. We see

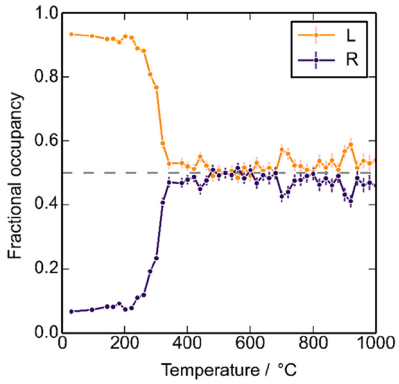

Figure 4. Variation of O3 oxygen fractional occupancies with increasing temperature. The orange and purple lines represent the fractions of L and R chains (as defined in Figure 1), respectively

that the phase transition observed in the neutron diffraction data and the thermal expansion data is accompanied by a gradual change from ordered chains pointing in predominantly one direction to an equal distribution of chains pointing in both directions.

Below the phase transition, the occupancies of the R and L chains refine to 0.07 and 0.93, respectively. This suggests that the chain ordering is not complete, even at room temperature, similar to that reported for $La_{2-x}Ba_xMn_2O_5$ brownmillerites.[35] In SSGO, this manifests in the small overcalculation of the (112) and (121) reflections in the room-temperature neutron diffraction data when using an *I*2*mb* model. The exact ratio of R to L chains is likely to be dependent on thermal history, so this finding may be specific to this particular sample; however, it suggests that disorder can be incorporated into the low-temperature structure, which could have implications on the conductivity of SSGO.

The phase transition elucidated here was previously detected and reported by Corallini et al.[11] from a seven-temperature powder neutron diffraction experiment, precluding its detailed characterization. Corallini et al.[11] also report $^{18}O/^{16}O$ isotope exchange measurements that suggest the onset for oxide ion mobility from 550 °C. The fact that the $(GaO_{4/2})_\infty$ chain rearrangement (which mainly involves structural changes of the oxygen atoms along the crystallographic *a*-axis) precedes the onset of oxide ion conductivity (which occurs mainly via vacancy migration along this direction) suggests that, if the two processes are interdependent, the former enhances the latter but does not act as a trigger mechanism.

DOI: 10.1021/acs.chemmater.9b02051
Chem. Mater. 2019, 31, 7395−7404

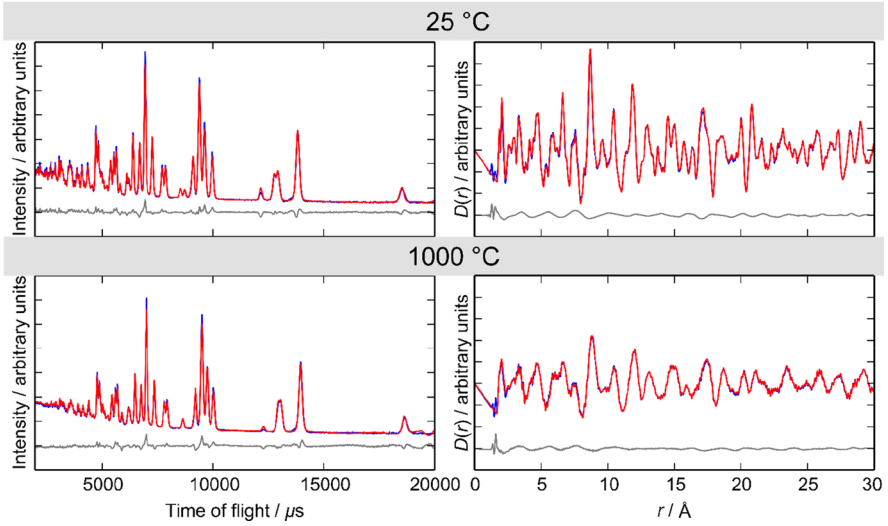

Figure 5. Fits to the Bragg (left) and PDF data (right) of SSGO at 25 and 1000 °C. Observed and calculated intensities and the difference between them are shown in blue, red, and gray, respectively. Final combined R_p values for the 25 and 1000 °C fits are 3.86 and 3.51%, respectively.

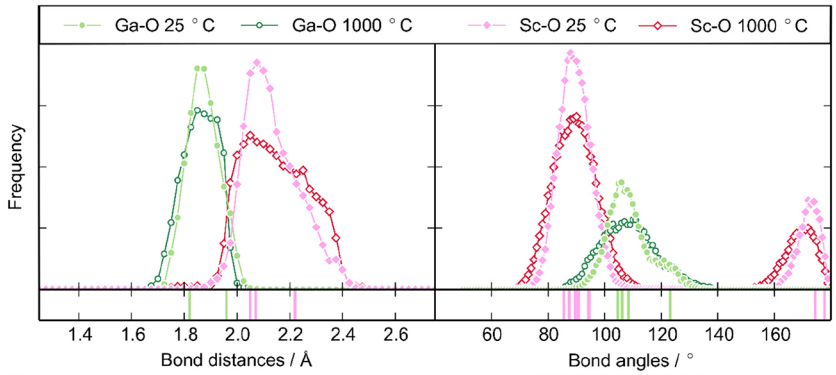

Figure 6. Distributions of bond lengths (left) and angles (right) of the refined supercell models at high and low temperatures. Tick marks in the lower panels show the average-structure values from the *I2mb* model.

Local Structure. There have been few total scattering local structure studies of brownmillerite-type oxides reported in the literature.[36−39] In the present work, the local structure of SSGO was investigated by simultaneously fitting the experimental neutron pair distribution function (PDF) and Bragg data with a large-box model in Topas Academic. For the room-temperature data, the *I2mb* model from Corallini et al.[11] was expanded to an approximately isotropic 12 × 4 × 12 (68.508 × 60.655 × 71.014 Å) supercell containing 20 736 atoms. For the 1000 °C data, a model was generated in which entire chains randomly pointed left or right along the *a*-axis. The positions of each atom were refined against the data, subject to penalties to retain sensible local coordination of GaO_4 and ScO_6 polyhedra and constraints to prevent large atomic shifts during initial cycles. To allow for thermal expansion, the penalties were only applied if bond lengths deviated from expected values by >0.05 Å.

Both models give excellent fits to their respective Bragg and PDF data at both long and short length scales (Figure 5). This suggests that the local structure is very similar to the average low-temperature structure both before and after the phase transition. In fact, the root-mean-square displacement from the starting structure (derived from the average crystallographic structure) increases only a small amount from 0.185 to 0.281 Å across this temperature range. This is illustrated by the cloud plots in Figure S7 and suggests that the local distortions within the long-range disordered $(GaO_{4/2})_\infty$ chains are relatively small.

There are noticeable differences between the high- and low-temperature data in the Bragg patterns, most obviously the intensity of the (112) and (121) peaks, which has already been attributed to the *I2mb-Imma* phase transition. However, the PDF gains no new features at high temperature and shows mainly the expected peak broadening due to increased thermal motion. Simulated patterns show that there are only minor differences between the PDF of the two forms of SSGO, and we therefore did not attempt to extract further information relating to chain disorder, such as the interplane versus intraplane ordering[35] discussed in other brownmillerites, from the PDF data.

Histograms of bond lengths and angles of the final large-box models are shown in Figure 6. The bond-length distribution of Ga−O bonds (green data points) remains relatively unchanged between room and high temperature, whereas the Sc−O distribution (red data points) visibly broadens with the mean bond length increasing from 2.146 to 2.159 Å. This analysis implies that GaO_4 tetrahedra are relatively rigid units, undergoing chain reorientation without significant deformation, and the ScO_6 octahedra likely distort to accommodate this motion. In fact, Ga−O mean distances in Figure 6 reduce

DOI: 10.1021/acs.chemmater.9b02051
Chem. Mater. 2019, 31, 7395−7404

from 1.890 to 1.871 Å on heating even in the local model. The regularization of tetrahedra at high temperature leading to more similar Ga−O3 and Ga−O2 bond lengths could contribute to this.[40]

The bond-angle distributions for both polyhedra broaden with temperature but remain centered around the crystallographic values, indicating that the shape of MO_n polyhedra is relatively unaffected by the transition. We note that bond-angle distributions of GaO_4 polyhedra show the expected departure from tetrahedral geometry with a significantly larger O2−Ga−O2 angle compared to others (O2 links to Sc layers). One important observation is that the Sc−O average bond length from Rietveld fitting does not show the same increase as the PDF model but, instead, remains almost constant; i.e., Sc−O bonds lengthen in the local model but are unchanged in the average structure. This reflects the local correlated motion of ScO_6 octahedra, which leads to the well-known apparent shortening of bonds when harmonic displacement parameters are used to describe the average structure.[41−43]

Inelastic Neutron Scattering. The inelastic neutron scattering of SSGO was measured between room temperature and 1000 °C up to a maximum energy transfer of 100 meV. $S(\omega)$ plots, given in the Supporting Information, show no quasielastic broadening around the elastic line on either IN6 (ps time scales) or IN16B (ns time scales).

The former instrument allows measurements of both inelastic and quasielastic scattering. The inelastic neutron scattering (INS) is measured as neutron energy gain at higher temperatures. The quasielastic neutron scattering (QENS) signal arises as a result of small energy exchanges between the incident neutrons and stochastic dynamic processes in a material. Especially when coupled with simulations, the analysis of QENS spectra enables one to differentiate long-range diffusion from localized motion processes and extract quantitative information such as activation energies, diffusion jump lengths, and lifetimes. Historically, the studies of oxide ion conductors by this technique have been hindered by the fact that oxygen is an essentially pure coherent scatterer of neutrons, meaning that the information about self-diffusion can be difficult to extract. However, recent advances in instruments (incident flux, detection efficiency, and access to longer diffusion time scales) have rendered studies of ionic diffusion in oxide ions conductors possible, although they remain challenging. For example, a combined use of QENS and ab initio molecular dynamics (AIMD) simulations gave the first direct observation of oxide ion dynamics in $La_2Mo_2O_9$.[44] This work provided the first proof of the proposal, put forward in the earlier crystallographic work,[45] that oxide ion diffusion in $La_2Mo_2O_9$ relied crucially on the flexibility of the coordination environment around Mo^{6+} and its propensity to support variable coordination numbers. Very recently, QENS and AIMD were used as complementary methods to directly observe oxide ion dynamics in bismuth vanadate $Bi_{0.913}V_{0.087}O_{1.587}$, which shows exceptional oxide ion conductivity at low temperatures.[46] This study revealed three dynamic processes in the material: a slow diffusion process through the Bi−O sublattice, a fast localized process within the VO_x coordination spheres, and exchanges of the oxide ions between the two sublattices. In addition to these examples of successful applications of QENS and simulations to structurally complex oxide ion conductors, there have also been studies of δ-Bi_2O_3, elucidating the high oxide ion mobility in the narrow stability region of this phase.[47,48]

In the case of SSGO, the existence of dynamic processes in the temperature range studied has been suggested by isotope exchange measurements[11] and demonstrated by our conductivity measurements (see later). The absence of an observed QENS signal therefore implies that the oxide ion dynamics in SSGO do not occur on the time scale of either IN16B or IN6 instrument, or that the dynamics are not sufficiently pronounced to generate an observable QENS signal owing to the essentially fully coherent nature of the oxygen scattering cross section.[44,46,49]

The phonon density of states (PDOS) was extracted from the spectrum measured on IN6 and is shown in Figure 7 along

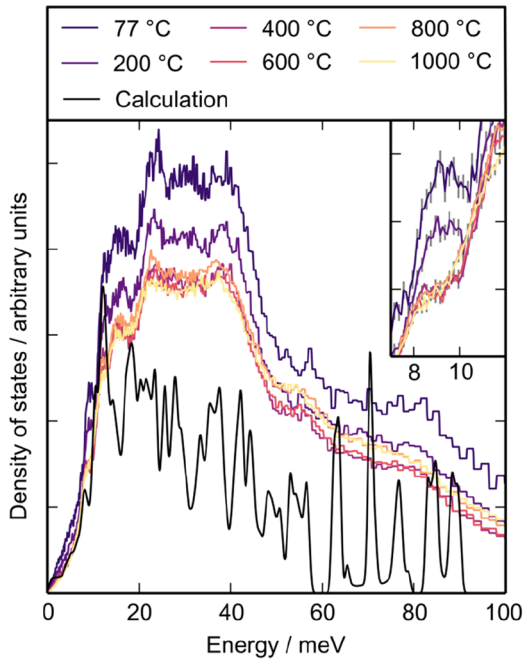

Figure 7. Experimental and calculated phonon density of states of SSGO. The inset shows a zoom of the low-energy region with associated error bars in gray. Note that the calculated and experimental curves are not normalized to each other.

with the PDOS from ab initio calculations. The overall shape is similar to that of $Sr_2Fe_2O_5$ and $Ca_2Fe_2O_5$,[10] and we observe a low-energy feature centered at 9.4 meV, which is also comparable with that seen in these other phases. A DFT phonon calculation was performed to investigate the distortions associated with this peak. The calculated PDOS reproduces the low-energy region very well and shows that a number of motions contribute to the peak at 9.4 meV. These predominantly involve the tetrahedral and octahedral layers sliding over each other along the [100] and [001] directions. This includes the concerted motion of tetrahedra back and forth along the proposed conduction channel (animations and phonon dispersion curves are available in the Supporting Information). As expected for a low-energy mode, they include minimal distortions of more rigid GaO_4 groups; instead, the ScO_6 octahedra deform and tilt slightly to accommodate the motion. This supports the conclusions from the local structure study with respect to the relative rigidity of the polyhedral layers.

The low-energy phonon modes seen in SSGO are different to those reported for $(Sr,Ca)_2Fe_2O_5$, which are associated with an asymmetric O2−Fe−O2 vibration along [010] leading to

DOI: 10.1021/acs.chemmater.9b02051
Chem. Mater. 2019, 31, 7395−7404

the lengthening of Fe−O2 bonds and the destabilization of the O2 site. An equivalent mode does occur in SSGO but at the higher energy of 16 meV, compared to 7 meV for $Sr_2Fe_2O_5$, again reflecting the more rigid nature of the structure as a whole.

The peak at 9.4 meV in the PDOS of SSGO softens to 8.2 meV between 200 and 400 °C. This is similar to softening seen in $Ca_2Fe_2O_5$,[10] and likewise, it appears to be connected to the phase transition involving the reorientation of the tetrahedral chain. The softening of a mode indicates that the relevant portion of the structure becomes more flexible.[50] Our local structure investigations show that the Sc−O bond-length distribution shifts toward longer bonds at high temperature, with a significantly higher proportion of bonds longer than 2.2 Å compared to room temperature. This would be consistent with the changes in the PDOS as ScO_6 distortions are involved in the modes assigned to this energy region.

Conductivity. Complex impedance plots for SSGO consisted of two partially overlapping semicircles with capacitances of $\sim 10^{-12}$ and $\sim 10^{-10}$ F/cm for the high- and low-frequency responses, respectively (Figure S9). Capacitances were calculated using the standard relationship $\omega RC = 1$ at the arc maximum and are consistent with the bulk and grain boundary responses.[51] At lower temperatures the total resistance could not be determined reliably due to noisy data at low frequencies, so the bulk conductivity is plotted in Figure 8. No electrode response was observed at any temperature (the same as in the SSGO single-crystal measurement[19]).

The Arrhenius curve of the bulk conductivity of SSGO in air (Figure 8) shows a modest conductivity, reaching 6×10^{-6} S cm^{-1} at 600 °C. As expected, the conductivity reported for the single-crystal cubic SSGO is higher than that of the polycrystalline orthorhombic SSGO because of the microstructure (higher density) and higher intrinsic disorder (presence of equivalent sites via which the ionic diffusion occurs).[52]

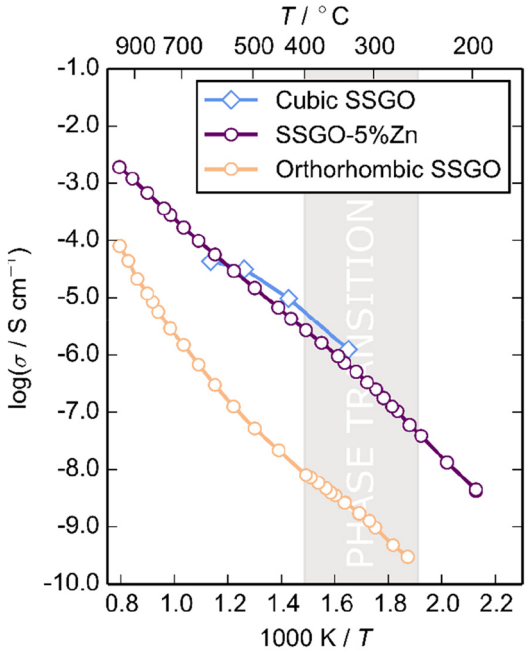

Figure 8. Arrhenius plots for the conductivity in air for brownmillerite-type orthorhombic SSGO, cubic SSGO (single-crystal measurement reported by Corallini et al.[19]), and orthorhombic SSGO-5%Zn. The gray shading indicates the temperature region of the phase transition in SSGO characterized by neutron diffraction in the present work.

With increasing temperature, there is first a small decrease in gradient that coincides with the *I2mb*−*Imma* structural phase transition (shaded temperature region in Figure 8). This occurs both in SSGO and the Zn-doped derivative, with the activation energies changing from 0.90(2) to 0.72(1) eV and from 0.98(1) to 0.87(1) eV for the two materials, respectively. As shown above, gradual dynamic reorientation of the chains occurs in this temperature region. This could assist the ionic mobility as the tetrahedral chain switching helps "push" migration along the [100] direction, or alternatively, the phase transition could induce distortion in the ScO_6 layer, which means that the barrier to vacancy hopping is lowered.

From ∼600 °C, the activation energy in SSGO increases to 1.65(3) eV. Additional impedance measurements in O_2, dry N_2, and wet N_2 (Figure S10) suggest that there is a proton contribution to the conductivity at low temperature, giving rise to ∼1/2 order of magnitude difference in the overall conductivity below 500 °C. TGA measurements (Figure S11) suggest a small water uptake (0.03−0.04 water molecules per SSGO formula unit). This can be compared to a difference of 2 orders of magnitude reported for $Sr_2Sc_{0.5}Ga_{1.5}O_5{\cdot}0.09H_2O$ in wet and dry atmospheres.[18] The conductivities in air and O_2 are essentially identical and only slightly higher than that in dry N_2; we therefore cannot rule out a small electronic contribution. The finding of additional contribution to the conductivity of SSGO is in contrast with the previously reported description of this material as a pure oxide ion conductor.[11,19] However, above ∼600 °C, the conductivities in N_2 (wet and dry), O_2, and air converge, indicating that oxide ion conductivity is predominant at high temperature. The increase in gradient in the SSGO Arrhenius curve therefore can be attributed to a change in dominant conduction process from proton to oxide ion conduction. This temperature coincides with the observation of oxide ion mobility by tracer diffusion measurements and is supported by ab initio molecular dynamics simulations.[11]

In an attempt to improve the conductivity of SSGO, some Sc^{3+} was replaced by Zn^{2+}, thereby creating additional oxygen vacancies in the octahedral layer. $Sr_2Sc_{0.95}Zn_{0.05}GaO_{4.975}$ was found to be a single-phase compound that retains the orthorhombic brownmillerite structure. The fit to its X-ray diffraction pattern (shown in the Supporting Information) obtained with the *I2mb* brownmillerite model was very good, and the cell parameters were a = 5.6931(5) Å, b = 15.1505(1) Å, and c = 5.9110(1) Å. The Zn-doping causes a contraction of the a-axis, lengthening of b, but barely any change in c. The conductivity of this compound was found to be significantly higher than that of the SSGO parent (Figure 8). An increase of ∼2 orders of magnitude was observed across a temperature range of 200−1000 °C, making SSGO-5%Zn comparable with the cubic single-crystal Sr_2ScGaO_5 reported by Corallini et al.[19]

Like SSGO, this derivative has a structural phase transition at ∼300 °C and the same subtle change in slope in the Arrhenius plot; beyond this temperature, the activation energy is 0.87(1) eV. The fact that the phase transition happens at the same temperature as undoped SSGO also means that the presence of vacancies in the octahedral layer is not strongly linked to the onset of chain reorientation.

For SSGO-5%Zn, the bulk and grain boundary semicircles were not separable, and the total conductivity is reported.

DOI: 10.1021/acs.chemmater.9b02051
Chem. Mater. 2019, 31, 7395−7404

SSGO-5%Zn also shows a similar contribution from proton conductivity to SSGO, i.e., the increase in conductivity upon changing from a dry to wet atmosphere is again ~1/2 an order of magnitude (Figure S10). In this case, however, the conductivity in wet N_2 does not exceed that in air and there is no further change in gradient above 400 °C. This suggests that oxide ion conduction is the dominant conduction process across the measured temperature range. The addition of extrinsic defects (generated by Zn^{2+} doping) increases the conductivity and decreases the activation energy of oxide ion conduction, implying that vacancies in the octahedral layer play an important role in the oxide ion migration mechanism.

Conductivity and Structure. In general, the modest ionic conductivity of SSGO can be attributed to the high degree of order in the structure. The best-performing conductors have a large free volume, contain many intrinsic oxygen defects (e.g., 25% of O sites in δ-Bi_2O_3 are vacant relative to the fluorite structure,[53] and 12.5% in pyrochlore-type oxide ion conductors;[54] good apatite-type oxide ion conductors contain up to 3.7% oxide ion interstitials[49,55]), or have cations that support a variety of coordination environments.[44−46,49,56−58] This provides numerous, low-energy migration pathways coupled with an abundance of charge carriers. In contrast, our local structure analysis has shown that SSGO has relatively rigid polyhedra with each cation having a strong preference for only one coordination environment[59] as well as anisotropic conduction channels. While the structure has many vacant sites, molecular dynamics simulations show that these are not readily occupied as no oxide ion migration from the octahedral layer to the tetrahedral layer is observed,[11] in agreement with the low mobility that can be inferred from our conductivity measurements. This is different from the conduction mechanism in the more highly conducting $Sr_2Fe_2O_5$, where simulations show the oxide ions on the O2 crystallographic sites migrating to vacant sites.[10,17] The phonon calculation in this work shows that the lattice dynamics thought to facilitate this motion occurs at a higher energy in SSGO (16 versus 7 meV). The only motion resembling oxide ion migration observed in SSGO simulations was the concerted reorientation of $(GaO_{4/2})_\infty$ chains, but this does not provide a long-range diffusion pathway; oxide ions can switch back and forth between the two local configurations. A different process is necessary for long-range conduction.

The oxide ion conduction mechanism in $Ba_2In_2O_5$ has been ascribed to the formation of oxygen Frenkel pairs made by removing an O1 from the octahedral layer in favor of a vacant position in the tetrahedral layer. Consequently, the migration pathway is thought to occur either via the vacant sites, along the $(InO_{4/2})_\infty$ chains, or by vacancy hopping in the octahedral layer as in traditional perovskites. The lowest-energy pathway was calculated to be vacancy hopping in the octahedral layer (E_a = 1.21 vs 1.34 eV for the tetrahedral layer process).[60,61] A similar mechanism in SSGO could be responsible for the oxide ion conduction process. This would be consistent with the observations that only tetrahedral chain reorientation was seen in MD simulations; GaO_4 tetrahedra are more rigid than ScO_6 octahedra, suggesting that the octahedral layer can more easily accommodate vacancy formation and hopping; the overall conductivity is low because there are no vacancies in the octahedral layers other than those formed when there is sufficient thermal energy; and, finally, deliberately adding oxygen vacancies by Zn-doping increases the conductivity.

CONCLUSIONS

Brownmillerite-type Sr_2ScGaO_5 has been synthesized and investigated by X-ray and neutron scattering techniques in order to characterize its local and average structure. We have correlated structural features to the measured conductivity, synthesized a derivative compound with increased conductivity, and suggested a plausible conduction mechanism based on our findings.

The average structure of SSGO is orthorhombic brownmillerite from room temperature to at least 1000 °C, although it has a phase transition over the temperature range of 260−340 °C. This has been evidenced by a deviation from a smooth trend in thermal expansion behavior, the intensity loss of certain peaks in the neutron diffraction pattern, changes in refined oxygen site occupancies, softening of modes in the phonon density of states, and a small change in gradient in the log-plot of conductivity against temperature. Rietveld fitting of the neutron diffraction data showed a space group change from *I2mb* to *Imma* that corresponds to the $(GaO_{4/2})_\infty$ chains transitioning from an ordered state where they point in one specific direction to a disordered state where the relative orientation of each chain is random. Occupancies of the two chain orientations show that the *I2mb* ordering is not necessarily complete at room temperature, although this is likely to be dependent on a sample's thermal history. The disordering of the tetrahedral chains was found to influence conductivity, as demonstrated by the decrease in activation energy after the transition. The temperature at which this transition occurs was found to be unchanged when 1.25% vacancies were introduced in the octahedral layer.

The local structure of SSGO is very similar to the average, with narrow bond-length and bond-angle distributions observed even at high temperature. This reflects the relatively rigid nature of the polyhedra. The most noticeable change between low and high temperature was the increase in both the mean value and spread of Sc−O bonds lengths compared to the Ga−O distribution. We have interpreted this as the GaO_4 being more rigid, such that the ScO_6 must distort to accommodate the tetrahedra reorienting above the phase transition. This description is consistent with our phonon calculations, which showed a low-energy mode involving small ScO_6 distortions consistent with the mode that softens at the phase transition.

The conductivity of SSGO is modest at 6×10^{-6} S cm^{-1} at 600 °C and is predominantly ionic in nature, although a proton contribution was observed at low temperature. The overall low conductivity can be explained by the lack of coordination flexibility in the structure causing the movement of oxide ions from ScO_6 to the vacant sites in tetrahedral layers to be unfavorable. A significant increase in conductivity and lowering of the activation energy was achieved by adding extrinsic vacancies into the octahedral layer by Zn-doping. This leads us to suggest that vacancy hopping in the octahedral layer is responsible for oxide ion conduction in these compounds.

ASSOCIATED CONTENT

Supporting Information

The Supporting Information is available free of charge on the ACS Publications website at DOI: 10.1021/acs.chemmater.9b02051.

Refined structural parameters for SSGO from neutron data; Rietveld refinement fit to X-ray diffraction patterns

DOI: 10.1021/acs.chemmater.9b02051
Chem. Mater. 2019, 31, 7395−7404

for SSGO and SSGO-5%Zn; variable-temperature neutron diffraction data showing peak changes at the phase transition; thermal expansion data for SSGO-5% Zn; $S(\omega)$ spectra for SSGO from IN6 and IN16b; elastic and inelastic fixed window scans for SSGO on IN16b; cloud plots showing the local polyhedral environments from the large-box fitting; phonon dispersion curves; a representative complex impedance plot; Arrhenius-type conductivity plots under different atmospheres; and a TGA trace (PDF)

Animations of key phonon modes (ZIP)

AUTHOR INFORMATION

ORCID

Quentin Berrod: 0000-0003-3254-1779

Ivana Radosavljevic Evans: 0000-0002-0325-7229

Notes

The authors declare no competing financial interest.

ACKNOWLEDGMENTS

The authors acknowledge the Science and Technology Facilities Council (STFC) for access to neutron beamtime at ISIS and thank H. Playford for help on the POLARIS instrument. We also acknowledge Institut Laue Langevin for neutron beamtime, data from which is available at DOI: 10.5291/ILL-DATA.7-03-171. I.R.E. acknowledges the Royal Society and the Leverhulme Trust for the award of a Senior Research Fellowship (SRF\R1\180040). Finally, we acknowledge Durham University for use of the Hamilton supercomputer and EPSRC Grant EP/P022782/1 for Archer supercomputer time.

REFERENCES

(1) Goodenough, J. B.; Ruiz-Diaz, J. E.; Zhen, Y. S. Oxide-Ion Conduction in $Ba_2In_2O_5$ and $Ba_3In_2MO_8$ (M = Ce, Hf, or Zr). *Solid State Ionics* **1990**, *44* (1−2), 21−31.

(2) Goodenough, J. B.; Manthiram, A.; Kuo, J. F. Oxygen Diffusion in Perovskite-Related Oxides. *Mater. Chem. Phys.* **1993**, *35* (3−4), 221−224.

(3) Jijil, C. P.; Unni, S. M.; Sreekumar, K.; Devi, R. N. Disordered Brownmillerite $Ba_2InCeO_{5+\delta}$ with Enhanced Oxygen Reduction Activity. *Chem. Mater.* **2012**, *24* (14), 2823−2828.

(4) Thundiyil, S.; Kurungot, S.; Devi, R. N. Bifunctional Oxygen Reduction and Evolution Activity in Brownmillerites $Ca_2Fe_{(2-x)}Co_xO_5$. *ACS Omega* **2019**, *4* (1), 31−38.

(5) Li, G.; Chen, W.; Wang, Y.; Duhan, B. Electronic Structure, Photoluminescence and Phosphorescence Properties in $Sr_2ScGaO_5:Sm^{3+}$. *Dyes Pigm.* **2018**, *157*, 259−266.

(6) Speakman, S. A.; Richardson, J. W.; Mitchell, B. J.; Misture, S. T. In-Situ Diffraction Study of $Ba_2In_2O_5$. *Solid State Ionics* **2002**, *149* (3−4), 247−259.

(7) Didier, C.; Claridge, J.; Rosseinsky, M. Crystal Structure of Brownmillerite Ba_2InGaO_5. *J. Solid State Chem.* **2014**, *218*, 38−43.

(8) Schwartz, M.; Link, B. F.; Sammells, A. F. New Brownmillerite Solid Electrolytes. *J. Electrochem. Soc.* **1993**, *140*, L62−L63.

(9) Yao, T.; Uchimoto, Y.; Kinuhata, M.; Inagaki, T.; Yoshida, H. Crystal Structure of Ga-Doped $Ba_2In_2O_5$ and Its Oxide Ion. *Solid State Ionics* **2000**, *132*, 189−198.

(10) Paulus, W.; Schober, H.; Eibl, S.; Johnson, M.; Berthier, T.; Hernandez, O.; Ceretti, M.; Plazanet, M.; Conder, K.; Lamberti, C. Lattice Dynamics To Trigger Low Temperature Oxygen Mobility in Solid Oxide Ion Conductors. *J. Am. Chem. Soc.* **2008**, *130*, 16080−16085.

(11) Corallini, S.; Ceretti, M.; Silly, G.; Piovano, A.; Singh, S.; Stern, J.; Ritter, C.; Ren, J.; Eckert, H.; Conder, K.; et al. One-Dimensional Oxygen Diffusion Mechanism in Sr_2ScGaO_5 Electrolyte Explored by Neutron and Synchrotron Diffraction, ^{17}O NMR, and Density Functional Theory Calculations. *J. Phys. Chem. C* **2015**, *119* (21), 11447−11458.

(12) Nemudry, A.; Weiss, M.; Gainutdinov, I.; Boldyrev, V.; Schöllhorn, R. Room Temperature Electrochemical Redox Reactions of the Defect Perovskite $SrFeO_{2.5+x}$. *Chem. Mater.* **1998**, *10*, 2403−2411.

(13) Hibino, M.; Harimoto, R.; Ogasawara, Y.; Kido, R.; Sugahara, A.; Kudo, T.; Tochigi, E.; Shibata, N.; Ikuhara, Y.; Mizuno, N. A New Rechargeable Sodium Battery Utilizing Reversible Topotactic Oxygen Extraction/Insertion of $CaFeO_z$ ($2.5 \leq z \leq 3$) in an Organic Electrolyte. *J. Am. Chem. Soc.* **2014**, *136* (1), 488−494.

(14) Shaula, A. L.; Pivak, Y. V.; Waerenborgh, J. C.; Gaczyński, P.; Yaremchenko, A. A.; Kharton, V. V. Ionic Conductivity of Brownmillerite-Type Calcium Ferrite under Oxidizing Conditions. *Solid State Ionics* **2006**, *177* (33−34), 2923−2930.

(15) Patrakeev, M. V.; Leonidov, I. A.; Kozhevnikov, V. L.; Kharton, V. V. Ion-Electron Transport in Strontium Ferrites: Relationships with Structural Features and Stability. *Solid State Sci.* **2004**, *6*, 907−913.

(16) Leonidov, I. A.; Patrakeev, M. V.; Bahteeva, J. A.; Poholok, K. V.; Filimonov, D. S.; Poeppelmeier, K. R.; Kozhevnikov, V. L. Oxygen-Ion and Electron Conductivity in $Sr_2(Fe_{1-x}Ga_x)_2O_5$. *J. Solid State Chem.* **2006**, *179* (10), 3045−3051.

(17) Auckett, J. E.; Studer, A. J.; Pellegrini, E.; Ollivier, J.; Johnson, M. R.; Schober, H.; Miiller, W.; Ling, C. D. Combined Experimental and Computational Study of Oxide Ion Conduction Dynamics in $Sr_2Fe_2O_5$ Brownmillerite. *Chem. Mater.* **2013**, *25* (15), 3080−3087.

(18) Chernov, S. V.; Dobrovolsky, Y. A.; Istomin, S. Y.; Antipov, E. V.; Grins, J.; Svensson, G.; Tarakina, N. V.; Abakumov, A. M.; Van Tendeloo, G.; Eriksson, S. G.; et al. Sr_2GaScO_5, $Sr_{10}Ga_6Sc_4O_{25}$, and $SrGa_{0.75}Sc_{0.25}O_{2.5}$: A Play in the Octahedra to Tetrahedra Ratio in Oxygen-Deficient Perovskites. *Inorg. Chem.* **2012**, *51* (2), 1094−1103.

(19) Corallini, S.; Ceretti, M.; Cousson, A.; Ritter, C.; Longhin, M.; Papet, P.; Paulus, W. Cubic Sr_2ScGaO_5 Perovskite: Structural Stability, Oxygen Defect Structure, and Ion Conductivity Explored on Single Crystals. *Inorg. Chem.* **2017**, *56* (5), 2977−2984.

(20) Ceretti, M.; Corallini, S.; Paulus, W. Influence of Phase Transformations on Crystal Growth of Stoichiometric Brownmillerite Oxides: Sr_2ScGaO_5 and $Ca_2Fe_2O_5$. *Crystals* **2016**, *6* (11), 146.

(21) Rietveld, H. M. A Profile Refinement Method for Nuclear and Magnetic Structures. *J. Appl. Crystallogr.* **1969**, *2* (2), 65−71.

(22) Coelho, A.; Evans, J. S. O.; Evans, I. R.; Kern, A.; Parsons, S. The TOPAS Symbolic Computation System. *Powder Diffr.* **2011**, *26*, S22−S25.

(23) Leineweber, A.; Dinnebier, R.; Evans, J. S. O. *Rietveld Refinement, Practical Powder Diffraction Pattern Analysis Using TOPAS*; De Gruyter: 2018.

(24) Stinton, G. W.; Evans, J. S. O. Parametric Rietveld Refinement. *J. Appl. Crystallogr.* **2007**, *40* (1), 87−95.

(25) Soper, A. K. *GudrunN and GudrunX: Programs for Correcting Raw Neutron and X-Ray Diffraction Data to Differential Scattering Cross Section*; Report RAL-TR-2011-013; STFC Rutherford Appleton Laboratory: 2011.

(26) Arnold, O.; Bilheux, J. C.; Borreguero, J. M.; Buts, A.; Campbell, S. I.; Chapon, L.; Doucet, M.; Draper, N.; Ferraz Leal, R.; Gigg, M. A.; et al. Mantid—Data Analysis and Visualization Package for Neutron Scattering and μ SR Experiments. *Nucl. Instrum. Methods Phys. Res., Sect. A* **2014**, *764*, 156−166.

(27) Tucker, M. G.; Keen, D. A.; Dove, M. T.; Goodwin, A. L.; Hui, Q. RMCProfile: Reverse Monte Carlo for Polycrystalline Materials. *J. Phys.: Condens. Matter* **2007**, *19* (33), 335218.

(28) Frick, B.; Combet, J.; Van Eijck, L. New Possibilities with Inelastic Fixed Window Scans and Linear Motor Doppler Drives on High Resolution Neutron Backscattering Spectrometers. *Nucl. Instrum. Methods Phys. Res., Sect. A* **2012**, *669*, 7−13.

(29) Richard, D.; Ferrand, M.; Kearley, J. LAMP, the Large Array Manipulation Program. *J. Neutron Res.* **1996**, *4*, 33−39.

DOI: 10.1021/acs.chemmater.9b02051
Chem. Mater. 2019, 31, 7395−7404

(30) Clark, S. J.; Segall, M. D.; Pickard, C. J.; Hasnip, P. J.; Probert, M. J.; Refson, K.; Payne, M. C. First Principles Methods Using CASTEP. *Z. Kristallogr. - Cryst. Mater.* **2005**, *220* (5/6), 567−570.
(31) Refson, K.; Tulip, P. R.; Clark, S. J. Variational Density-Functional Perturbation Theory for Dielectrics and Lattice Dynamics. *Phys. Rev. B: Condens. Matter Mater. Phys.* **2006**, *73* (15), 155114.
(32) Perdew, J.; Burke, K.; Ernzerhof, M. Generalized Gradient Approximation Made Simple. *Phys. Rev. Lett.* **1996**, *77* (18), 3865−3868.
(33) Lejaeghere, K.; Bihlmayer, G.; Björkman, T.; Blaha, P.; Blügel, S.; Blum, V.; Caliste, D.; Castelli, I. E.; Clark, S. J.; Dal Corso, A.; et al. Reproducibility in Density Functional Theory Calculations of Solids. *Science* **2016**, *351* (6280), aad3000.
(34) *Jmol: An Open-Source Java Viewer for Chemical Structures in 3D*; http://jmol.sourceforge.net/.
(35) Parsons, T. G.; D'Hondt, H.; Hadermann, J.; Hayward, M. A. Synthesis and Structural Characterization of $La_{1-x}A_xMnO_{2.5}$ (A = Ba, Sr, Ca) Phases: Mapping the Variants of the Brownmillerite Structure. *Chem. Mater.* **2009**, *21* (22), 5527−5538.
(36) Mancini, A.; Shin, J. F.; Orera, A.; Slater, P. R.; Tealdi, C.; Ren, Y.; Page, K. L.; Malavasi, L. Insight into the Local Structure of Barium Indate Oxide-Ion Conductors: An X-Ray Total Scattering Study. *Dalt. Trans.* **2012**, *41* (1), 50−53.
(37) King, G.; Ramezanipour, F.; Llobet, A.; Greedan, J. E. Local Structures of Sr_2FeMnO_{5+y} (y = 0, 0.5) and $Sr_2Fe_{1.5}Cr_{0.5}O_5$ from Reverse Monte Carlo Modeling of Pair Distribution Function Data and Implications for Magnetic Order. *J. Solid State Chem.* **2013**, *198*, 407−415.
(38) King, G.; Thompson, C. M.; Luo, K.; Greedan, J. E.; Hayward, M. A. Identifying the Local Structural Units in $La_{0.5}Ba_{0.5}MnO_{2.5}$ and $BaY_{0.25}Fe_{0.75}O_{2.5}$ through the Neutron Pair Distribution Function. *Dalt. Trans.* **2017**, *46*, 1145.
(39) Ramezanipour, F.; Greedan, J. E.; Siewenie, J.; Donaberger, R. L.; Turner, S.; Botton, G. A. A Vacancy-Disordered, Oxygen-Deficient Perovskite with Long-Range Magnetic Ordering: Local and Average Structures and Magnetic Properties of $Sr_2Fe_{1.5}Cr_{0.5}O_5$. *Inorg. Chem.* **2012**, *51* (4), 2638−2644.
(40) Evans, J. S. O. Negative Thermal Expansion Materials. *J. Chem. Soc., Dalton Trans.* **1999**, *19*, 3317−3326.
(41) Cox, E. G.; Cruickshank, D. W. J.; Smith, J. A. S. Crystal Structure of Benzene: A New Type of Systematic Error in Precision x-Ray Crystal Analysis. *Nature* **1955**, *175*, 766.
(42) Cruickshank, D. W. J. The Analysis of the Anisotropic Thermal Motion of Molecules in Crystals. *Acta Crystallogr.* **1956**, *9*, 754−756.
(43) Busing, W. R.; Levy, H. A. The Effect of Thermal Motion on the Estimation of Bond Lengths from Diffraction Measurements. *Acta Crystallogr.* **1964**, *17* (2), 142−146.
(44) Peet, J. R.; Fuller, C.; Frick, B.; Zbiri, M.; Piovano, A.; Johnson, M. R.; Evans, I. R. Direct Observation of Oxide Ion Dynamics in $La_2Mo_2O_9$ on the Nanosecond Timescale. *Chem. Mater.* **2017**, *29*, 3020−3028.
(45) Evans, I. R.; Howard, J. A. K.; Evans, J. S. O. The Crystal Structure of α-$La_2Mo_2O_9$ and the Structural Origin of the Oxide Ion Migration Pathway. *Chem. Mater.* **2005**, *17*, 4074−4077.
(46) Peet, J. R.; Fuller, C. A.; Frick, B.; Koza, M.; Johnson, M. R.; Piovano, A.; Evans, I. R. Insight into Design of Improved Oxide Ion Conductors: Dynamics and Conduction Mechanisms in the $Bi_{0.913}V_{0.087}O_{1.587}$Solid Electrolyte. *J. Am. Chem. Soc.* **2019**, *141* (25), 9989−9997.
(47) Mamontov, E. Fast Oxygen Diffusion in Bismuth Oxide Probed by Quasielastic Neutron Scattering. *Solid State Ionics* **2016**, *296*, 158−162.
(48) Wind, J.; Mole, R. A.; Yu, D.; Ling, C. D. Liquid-like Ionic Diffusion in Solid Bismuth Oxide Revealed by Coherent Quasielastic Neutron Scattering. *Chem. Mater.* **2017**, *29*, 7408−7415.
(49) Peet, J. R.; Chambers, M. S.; Piovano, A.; Johnson, M. R.; Evans, I. R. Dynamics in Bi(III)-Containing Apatite-Type Oxide Ion Conductors: A Combined Computational and Experimental Study. *J. Mater. Chem. A* **2018**, *6*, 5129−5135.
(50) Perrichon, A.; Piovano, A.; Boehm, M.; Zbiri, M.; Johnson, M.; Schober, H.; Ceretti, M.; Paulus, W. Lattice Dynamics Modified by Excess Oxygen in $Nd_2NiO_{4+\delta}$: Triggering Low-Temperature Oxygen Diffusion. *J. Phys. Chem. C* **2015**, *119* (3), 1557−1564.
(51) Irvine, J. T. S.; Sinclair, D. C.; West, A. R. Electroceramics: Characterization by Impedance Spectroscopy. *Adv. Mater.* **1990**, *2*, 132−138.
(52) Barsoukov, E.; Macdonald, J. R. *Impedance Spectroscopy: Theory, Experiment and Applications*, 2nd ed.; John Wiley & Sons: 2005.
(53) Drache, M.; Roussel, P.; Wignacourt, J. P. Structures and Oxide Mobility in Bi-Ln-O Materials: Heritage of Bi_2O_3. *Chem. Rev.* **2007**, *107* (1), 80−96.
(54) Wuensch, B.; Eberman, K. W.; Heremans, C.; Ku, E. M.; Onnerud, P.; Yeo, E. M. E.; Haile, S. M.; Stalick, J. K.; Jorgensen, J. D. Connection between Oxygen-Ion Conductivity of Pyrochlore Fuel-Cell Materials and Structural Change with Composition and Temperature. *Solid State Ionics* **2000**, *129* (1−4), 111−133.
(55) Tate, M. L.; Blom, D. A.; Avdeev, M.; Brand, H. E. A.; McIntyre, G. J.; Vogt, T.; Evans, I. R. New Apatite-Type Oxide Ion Conductor, $Bi_2La_8[(GeO_4)_6]O_3$: Structure, Properties, and Direct Imaging of Low-Level Interstitial Oxygen Atoms Using Aberration-Corrected Scanning Transmission Electron Microscopy. *Adv. Funct. Mater.* **2017**, *27* (8), 1605625.
(56) Kuang, X.; Green, M. A.; Niu, H.; Zajdel, P.; Dickinson, C.; Claridge, J. B.; Jantsky, L.; Rosseinsky, M. J. Interstitial Oxide Ion Conductivity in the Layered Tetrahedral Network Melilite Structure. *Nat. Mater.* **2008**, *7*, 498−504.
(57) Kuang, X.; Payne, J. L.; Farrell, J. D.; Johnson, M. R.; Evans, I. R. Polymorphism and Oxide Ion Migration Pathways in Fluorite-Type Bismuth Vanadate, $Bi_{46}V_8O_{89}$. *Chem. Mater.* **2012**, *24* (11), 2162−2167.
(58) Kuang, X.; Payne, J. L.; Johnson, M. R.; Evans, I. R. Remarkably High Oxide Ion Conductivity at Low Temperature in an Ordered Fluorite-Type Superstructure. *Angew. Chem., Int. Ed.* **2012**, *51* (3), 690−694.
(59) Waroquiers, D.; Gonze, X.; Rignanese, G. M.; Welker-Nieuwoudt, C.; Rosowski, F.; Göbel, M.; Schenk, S.; Degelmann, P.; André, R.; Glaum, R.; et al. Statistical Analysis of Coordination Environments in Oxides. *Chem. Mater.* **2017**, *29* (19), 8346−8360.
(60) Fisher, C. A. J.; Islam, M. S. Defect, Protons and Conductivity in Brownmillerite-Structured $Ba_2In_2O_5$. *Solid State Ionics* **1999**, *118* (3−4), 355−363.
(61) Fisher, C. A. J.; Islam, M. S.; Brook, R. J. A Computer Simulation Investigation of Brownmillerite-Structured $Ba_2In_2O_5$. *J. Solid State Chem.* **1997**, *128* (1), 137−141.

DOI: 10.1021/acs.chemmater.9b02051
Chem. Mater. 2019, 31, 7395−7404